nuclear fusion
IAEA

PAPER • OPEN ACCESS

A code-to-code benchmark for magneto-convection in a horizontal duct

To cite this article: Chiara Mistrangelo *et al* 2025 *Nucl. Fusion* **65** 116006

OPEN ACCESS
IOP Publishing | International Atomic Energy Agency
Nuclear Fusion
Nucl. Fusion **65** (2025) 116006 (18pp)
https://doi.org/10.1088/1741-4326/ae0800

A code-to-code benchmark for magneto-convection in a horizontal duct

Chiara Mistrangelo[1,*], Leo Bühler[1], Sergey Smolentsev[2], Alessandro Tassone[3], Guillermo G Fonfría[4], Yuchen Jiang[2], Lorenzo Melchiorri[3], Gerasimos Politis[5], Daniel Suarez[2] and Fernando R Urgorri[4]

[1] Karlsruhe Institute of Technology, Karlsruhe, Germany
[2] Oak Ridge National Laboratory, Oak Ridge, TN, United States of America
[3] Sapienza University of Rome, 00186 Rome, Italy
[4] National Fusion Laboratory, CIEMAT, Madrid 28040, Spain
[5] UKAEA, Abingdon, Oxfordshire OX14 3DB, United Kingdom of Great Britain and Northern Ireland

E-mail: chiara.mistrangelo@kit.edu

Received 9 June 2025, revised 20 August 2025
Accepted for publication 17 September 2025
Published 6 October 2025

Abstract

Liquid metals and magnetic fields are used in many technical applications such as metallurgy, crystal growth and nuclear fusion reactors. When an electrically conducting fluid moves in a magnetic environment, electric currents and electromagnetic forces are generated that affect velocity and pressure losses in the flow. These magnetohydrodynamic (MHD) interactions have to be investigated to optimize the engineering processes. The characteristics of MHD flows depend on the geometrical configuration, the strength of the applied magnetic field, the electrical properties of fluid and structural materials and the thermal conditions. In the so-called blankets for fusion reactors, where liquid metals are used to breed the plasma fuel component tritium and to extract the generated heat, magneto-convective flows play a crucial role in determining heat and mass transfer. Therefore, the availability of numerical codes to simulate this type of flow is mandatory and their validation is a necessary step to guarantee the reliability of the results. For that reason, a benchmark problem has been defined to simulate liquid metal flows in a horizontal rectangular duct heated from below and exposed to a non-uniform magnetic field. Results obtained by five research groups using different codes are compared.

Keywords: fusion blankets, liquid metals, magneto-convection, benchmark, code-to-code comparison

(Some figures may appear in colour only in the online journal)

* Author to whom any correspondence should be addressed.

1. Introduction

The use of liquid metals such as lead-lithium (PbLi) is a promising option for breeding blankets in future fusion power plants, where the fuel component tritium is produced from the interaction of high-energy fusion neutrons with the alloying component lithium. The liquid metal serves also as a neutron multiplier and its high thermal conductivity makes it an ideal heat transfer medium. The hot fusion plasma is confined in the vacuum vessel, away from the structural materials, by an intense magnetic field. The drawback of using liquid metals in a magnetic environment is the occurrence of magnetohydrodynamic (MHD) interactions between the moving electrically conducting fluid and the strong applied magnetic field. These result in high pressure drops, non-uniform flow patterns, suppression of 3D turbulence, and degradation of heat transfer.

A reliable engineering design of fusion blankets requires accurate prediction of MHD flows [1]. Numerical tools have to prove their capability to simulate different types of flows driven by pressure differences or buoyancy forces in fluid domains that are electrically and thermally coupled by leakage currents and heat flux exchanged through conductive walls. MHD simulations for fusion applications are particularly challenging since, due to the strong imposed magnetic field, the flow is dominated by electromagnetic forces. This leads to the formation of extremely thin boundary layers or internal viscous-inertial layers that require adequate mesh resolution. In addition, the numerical treatment of the governing equations results in stiff systems of algebraic equations where small initial uncertainties can be amplified leading to a lack of convergence of the iterative methods or the occurrence of high local numerical errors.

In recent years, significant progress has been made in the numerical modeling of MHD flows in strong magnetic fields through the use of advanced current-conservative schemes [2, 3] and the rapid development of high-performance computing, which provides the necessary computational resources. Therefore, numerical methods have become the preferred tool for MHD analysis of liquid metal flows in fusion applications. To ensure the reliability and accuracy of MHD codes developed worldwide, Smolentsev *et al* [4] proposed a systematic verification and validation of the numerical tools presently used by the fusion community for the analysis of liquid metal flows. The latter authors suggested benchmark cases for a number of MHD problems for which either exact or asymptotic analytical solutions exist (fully established steady-state laminar flows), or where well documented experimental data is available (3D flows in fringing magnetic fields, unstable time-dependent flows and flows with heat transfer). Since the publication of the latter reference, a number of magneto-convective flows has been studied theoretically and experimentally (see e.g. the comprehensive review paper by Zikanov *et al* [5]) for fluids such as mercury, gallium, GaInSn, sodium, sodium-potassium. However, experimental data obtained by employing the fusion-relevant fluid PbLi is rare [6]. With the aim of broadening the experimental data base for MHD heat transfer problems with PbLi, new experimental campaigns have been planned using the MaPLE facility at the Karlsruhe Institute of Technology (KIT) [7] in both vertical and horizontal channels under various thermal conditions. Results will represent a valuable data base for validation of numerical MHD codes.

In the meantime, while experiments are being prepared, the present authors agreed on the continuation of an international code-to-code benchmark activity [8] motivated by the above-mentioned experiments. In the first part of the project, the buoyancy-opposed MHD flow was studied in a long vertical rectangular duct partially heated from a lateral wall. It was found that all considered codes could predict well the key flow features with moderate quantitative differences. Boundary layer separation and local flow reversal were observed depending on magnetic field strength, imposed mean velocity and wall heat flux.

The present work complements previous investigations with a code-to-code comparison for heat transfer in PbLi flow in a horizontal square channel heated from below. The surface heat flux is applied on a portion of the lower wall of the duct in a region where the imposed horizontal magnetic field is uniform. We take also into account additional 3D effects that occur at the entrance and exit of the magnet, where the magnetic field varies between zero and a maximum value. The present problem is of particular interest because fluid layers heated from below develop an unstable density stratification, which may lead to flow instability and promote vortical flow near the heated wall, with implications for heat transfer.

In section 2, details about magnetic field distribution and thermal boundary conditions are given. Governing equations, scaling quantities, and dimensionless parameters characterizing the flow are defined in section 3. In section 4, the codes involved in the study are described and differences in the simulation set-ups are highlighted in order to facilitate the explanation of possible discrepancies observed during the comparison of the results discussed in section 5.

2. Problem description

We consider a liquid metal flow with mean velocity u_0 in a horizontal electrically and thermally conducting square duct, which is inserted in a non-uniform magnetic field. Geometry and reference coordinate system are shown in figure 1. The thickness of the wall is $t_w = 2{\cdot}10^{-3}$ m and the characteristic size of the channel is $a = 0.023$ m, which is the duct half-width in the direction of the applied magnetic field. The total length of the duct used for the simulations depends on the selected flow parameters and the given boundary conditions. Dimensions and set-up of the problem correspond to the ones of the experimental campaign that will be carried out in the PbLi MaPLE facility at KIT [7].

A homogeneous heat flux q'' is applied to the outer surface of the bottom wall of the channel for $-0.3\ \text{m} \leqslant x \leqslant 0.3\ \text{m}$, as marked by the red arrows in figure 1. Contours of magnetic field strength are plotted on the middle plane $y = 0$. For $|x| < 0.4$ m the magnetic field is constant, $B_y = B_0$, while for $|x| > 0.4$ m it varies rapidly and it tends to zero for $|x| > 1$ m. The magnetic field can be mathematically expressed

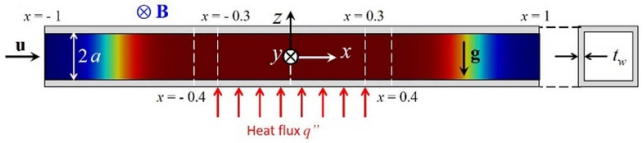

Figure 1. Geometry employed for simulation of magneto-convective flows in a square duct with electrically and thermally conducting wall. The thickness of the wall is indicated by t_w and the typical size of the duct by a. Coordinates are expressed in meters. Contours of magnetic field strength $B_y(x)$ are plotted on the plane $y = 0$.

by equation (1) derived by fitting values measured when preparing the experiments:

$$B_y(x) = \frac{1}{2}B_0\left[1 - \tanh\left(\frac{|x| - 0.7315}{0.1}\right)\right]. \quad (1)$$

3. Mathematical model and scaling quantities

The liquid metal magneto-convective flow is governed by the momentum equation, where the inertia force balances pressure, viscous, electromagnetic and buoyancy forces,

$$\rho_0\left(\frac{\partial}{\partial t} + \mathbf{u}\cdot\nabla\right)\mathbf{u} = -\nabla p + \rho_0\nu\nabla^2\mathbf{u} + \mathbf{j}\times\mathbf{B} - \rho_0\beta(\mathrm{T} - \mathrm{T}_0)\mathbf{g}, \quad (2)$$

and by mass conservation, $\nabla\cdot\mathbf{u} = 0$. In equation (2) the variables $\mathbf{u}$, p, $\mathbf{j}$, $\mathbf{B}$ and T indicate velocity, pressure, current density, magnetic field and temperature, and $\mathbf{g}$ is the acceleration due to gravity. The thermophysical properties of PbLi are ρ_0 (reference density), ν (kinematic viscosity), and β (thermal expansion coefficient).

Two source terms are present in equation (2), i.e. the electromagnetic Lorentz force, $\mathbf{j}\times\mathbf{B}$, and the buoyancy term due to density variations caused by temperature differences. The latter is expressed using the Boussinesq approximation, i.e. it is assumed that the dependence of density on temperature is restricted to the buoyancy term. This assumption is valid as long as we consider a small temperature range [9].

The current density $\mathbf{j}$ that determines with $\mathbf{B}$ the strength of the Lorentz force is obtained from Ohm's law

$$\mathbf{j} = \sigma(-\nabla\phi + \mathbf{u}\times\mathbf{B}). \quad (3)$$

Currents are driven by the gradient of an electric potential ϕ and a flow-induced electric field $\mathbf{u}\times\mathbf{B}$. The electric potential is determined by solving a Poisson equation derived from Ohm's law by imposing charge conservation $\nabla\cdot\mathbf{j} = 0$. Equations are written according to the inductionless approximation, which implies that the flow-induced magnetic field is negligible compared to the imposed one.

The temperature in equation (2) is calculated solving the energy balance equation:

$$\rho c_p\left(\frac{\partial}{\partial t} + \mathbf{u}\cdot\nabla\right)T = \nabla\cdot(k\nabla T). \quad (4)$$

Table 1. Selected comparison cases. The magnetic field strength (*Ha*) remains constant, while *Re* and *Gr* are different.

	Ha	*Re*	*Gr*	*Ri*
Case 1	235	3220	$1.42\cdot10^7$	1.37
Case 2	235	1073	$3.55\cdot10^7$	30.8

Equation (2) is used in the flow domain, while equations (3) and (4) refer to the multi-material domains of PbLi and surrounding stainless steel walls. In these equations, ρ is the density, σ the electrical conductivity, c_p the specific heat capacity, and k the thermal conductivity. These properties are taken at a reference temperature $T_0 = 300$ °C for PbLi and stainless steel according to [10, 11], respectively.

At the fluid-wall interface, continuity of wall normal current $j_n = j_{nw}$, electric potential $\phi = \phi_w$, temperature $T = T_w$, and heat flux $q'' = q''_w$ is imposed. The external surface of the duct is electrically insulating ($\partial_n\phi_w = 0$) and adiabatic ($\partial_n T_w = 0$), except for the heated area where the constant heat flux is applied. Conditions at the entrance and exit of the channel are specified in table 4.

The flow is governed by three non-dimensional parameters, i.e. Reynolds number *Re*, Hartmann number *Ha,* and Grashof number *Gr*:

$$Re = \frac{au_0}{\nu},\ Ha = B_0 a\sqrt{\frac{\sigma}{\rho\nu}},\ Gr = \frac{g\beta\Delta T a^3}{\nu^2}. \quad (5)$$

The Reynolds number and the square of the Hartmann number quantify the ratios of inertia and electromagnetic forces to the viscous forces, respectively. As alternative parameter the interaction parameter can be defined as $N = Ha^2/Re$, which expresses the relative importance of electromagnetic and inertia forces. The Grashof number gives a measure for the intensity of buoyant forces with respect to the viscous forces. A characteristic temperature difference ΔT is defined as $\Delta T = q''a/k$. Another useful parameter when dealing with thermal convection problems is the Richardson number $Ri = Gr/Re^2$ that represents the ratio of velocity scales associated with natural and forced convection in the flow.

For the present work, two cases have been simulated and compared, as listed in table 1. The strength of the magnetic field is kept constant (same *Ha*), while in Case 2 the velocity u_0 (*Re*) is reduced and the applied surface heat flux q'' (Gr) is increased.

It should be noted that in *Case 2* the Richardson number *Ri* is larger than in *Case 1* due to the smaller mean velocity. Hence, it is expected that in *Case 2* the forced convection is much weaker. Moreover, the combined parameter *Ri*/*N*, which gives a measure for the relative importance of buoyancy and Lorentz forces [5], suggests for *Case 1* (*Ri*/*N* = 0.0796) the occurrence of weak magneto convective effects and for *Case 2* (*Ri*/*N* = 0.596) a more complex interaction among buoyancy, electromagnetic and inertia forces.

Table 2. Numerical schemes used to discretize the equation terms: time-derivative $\partial/\partial t$, convective term $u\cdot\nabla$, ∇p, $\nabla\phi$, and Laplacian ∇^2.

Code	$\partial/\partial t$	u·∇	∇p, $\nabla\phi$	∇^2
FLUENT CIEMAT	1st order implicit	2nd order upwind	Gauss	Gauss
FLUENT UK	2nd order implicit	2nd order upwind	LS	
CFX	Backward Euler	Central	TLI	TLI
OF ORNL	Forward Euler	2nd order TVD	central	harmonic ϕ others linear
OF KIT	2nd order backward	Central	Gauss (p) 2nd LS (ϕ)	Gauss
COMSOL	2nd order backward	Streamline stabilization	Linear elements	2nd order elements

Table 3. Number of grid points along the three coordinates. $\Delta x/a$ indicates the normalized cell size in axial direction in the heated zone (HZ), i.e. for $|x|\leqslant 0.3$m, where for all simulations the mesh is uniform. The wall is indicated by W. Last column: numbers of points in Hartmann (Ha) and side (Side) layers.

Code	# x	$\Delta x/a$ HZ	# y	#z	CPU	in layers
FLUENT CIEMAT	unif. 165 (*Case 1*) unif. 141 (*Case 2*)	0.58 (*Case 1*) 0.709 (*Case 2*)	60 60 W:10	60 60 W:10	36	Ha: 7 Side: 7
FLUENT UK	non-unif. 287	0.217	86 W:13	86 W:13	120	Ha: 8 Side: 23
CFX	unif. 450	0.22	192 W:16	74 W:16	432	Ha: 7 Side: 15
OF ORNL	unif. 200 (*Case 1*) unif. 230 (*Case 2*)	0.435	62 W:8	52 W:7	16	Ha: 7 Side: 14
OF KIT	non-unif. 700	0.065	96 W:10	86 W:10	512	Ha: 8 Side: 16
COMSOL	300	0.261	60 W:10	60 W:10	32	Ha: 8 Side: 12

4. Numerical codes

In the following, the codes used to obtain the results discussed in section 5 are briefly described in order to highlight the differences in the set-up of the simulations, which could lead to discrepancies during the comparison. In the brackets, close to the names of the codes, it is indicated how we refer to the corresponding data in the legend of the figures presented in section 5 when the same code is used by different research groups.

Apart from the software COMSOL, which is a finite-element-based solver [12, 13], the other codes employed for the present study adopt a finite-volume method to solve the governing equations. All codes work on a hexahedral structured mesh, with points clustered towards the walls.

Numerical schemes for discretization of the terms in the equations, boundary conditions applied at inlet and outlet of the computational domain, and the number of points used to resolve the different regions in the channel are summarized in tables 2–4. The thickness of the boundary layers that develop along walls perpendicular and parallel to the magnetic field is defined according to $\delta_{\rm Ha} = aHa^{-1}$ and $\delta_{\rm Side} = aHa^{-1/2}$, respectively. The former is called Hartmann layer, and the latter is named side layer.

ANSYS CFX [14] The finite-difference equations are solved iteratively using a multigrid solver accelerated by the use of the incomplete factorization technique [15]. For discretization of gradients and Laplacian, a trilinear interpolation (TLI) with finite-element geometric shape function is applied. Local quantities (velocity, electric potential, current density, temperature) are monitored at 53 locations to assess

convergence of the transient run. Internal convergence criteria are set as a minimum of 2 loops, RMS residual lower than $5{\cdot}10^{-5}$. Adaptive time step size is used during the run with $\Delta t = 1.5{\cdot}10^{-2}$ s being the final value for both cases. Computations are performed on ENEA CRESCO6 cluster using 432 CPUs Intel(R) Xeon(R) Platinum 8160 2.10 GHz.

ANSYS FLUENT (FLUENT_CIEMAT) The standard pressure-based solver with PISO as pressure-velocity coupling scheme is employed. Time advancement is based on a first order implicit scheme with a time-step size of 10 ms for *Case 1* and 1 ms for *Case 2*. In both cases ten iterations per time-step were required. Additional buffer zones of 5% of the channel's length at the inlet and 5% (*Case 1*) or 10% (*Case 2*) in the outlet region were added compared to the original duct geometry. The simulations were run at the Turgalium cluster operated by CETA-Ciemat with 36-core nodes. Depending on the case, simulations run for 24 h to 2 week wall-clock time. This is due to both a difference in the time-step size and longer simulation time required in *Case 2* to obtain good time averages due to the oscillating nature of the flow.

ANSYS FLUENT (FLUENT_UK) A pressure-based coupled solver was utilized, incorporating second-order approximations for the pressure gradient. This upwind scheme necessitates cell-centered values for each cell and cell-centered gradients in the upstream cell. To evaluate these gradients, the least squares (LS) cell-based scheme was applied.

COMSOL [12, 16] A customized COMSOL model is used. The finite-volume equations are linearized with the Newton-Raphson method. The PARDISO direct solver is used to solve the linearized equations for pressure and velocity. For the temperature, a GMRES solver is employed combined with smoothed aggregation AMG method. For the electric potential, the conjugate gradient solver was chosen, with algebraic multigrid method. Simulations are performed on the fusion-comsol server at ORNL. Each case occupied 32 cores. The time interval was set to 0.05 s with a total physical time of 300s.

OpenFOAM Both research groups using this software employ a customized MHD solver in which the pressure—velocity coupling is based on the PISO algorithm. The pre-conditioned gradient algebraic solver is used for pressure, while the pre-conditioned bi-conjugate gradient solver for velocity and temperature. The solvers are developed by using two different version of OpenFOAM: foam-extend-4.0 *(OF_KIT)* and foam-extend-3.2 *(OF_ORNL)*.

OpenFOAM (*OF_ORNL*) [17] for discretization of convective terms the Van Leer total variation diminishing (TVD) scheme is used. The electric potential equation is solved using a conjugate gradient method together with the Cholesky preconditioner. The simulations ran for up to 500 s for *Case 1* and 600 s for *Case 2*, each requiring approximately 2 weeks of computational time.

The additional cells in *Case 2* are due to an extension of the domain by 15% of the channel length. Additionally, artificial viscosity was applied in the last 20% of the channel to avoid backflow from the outlet.

OpenFOAM (*OF_KIT*) [18] The electric potential equation is solved using the preconditioned bi-conjugate gradient method with Cholesky preconditioner. Simulations have been carried out on the Japan Fusion Reactor Simulator 1 (JFRS-1) with up to 512 CPU for the finest mesh (Processors: 2×20 cores Intel Xeon Gold 6148 2.4 GHz). Adaptive time step is employed with a final $\Delta t = 0.01$ s for the coarsest mesh and 0.004s for the finest grid. Three different mesh refinements have been used.

5. Discussion of the numerical results

It has been agreed that the comparison will focus mainly on the region that starts where the magnetic field begins to increase at the entrance of the magnet, i.e. at $x = -1$ m. It is expected that the inlet boundary conditions, which are applied further upstream, will not significantly affect the results for $x \geqslant -1$ m.

Concerning the outlet boundary conditions, it seems that an advective outflow condition, combined with a longer outlet channel, yields reasonable results. However, limitations in the definition of boundary conditions in commercial codes, may result in unphysical flow behavior at the outlet. An alternative to the advective condition when not available, is the use of an extended outlet duct, even longer than what has been used by other codes, or of an artificial high viscosity close to the exit (see table 4). As expected, the different inlet and outlet boundary conditions lead to dissimilarities among data computed with the different codes. Therefore, hereafter when discussing the results, deviations that can be directly ascribed to the boundary conditions are not always explicitly mentioned except if interesting general conclusions can be derived.

During the comparison of the results, data is distinguished by the reference names defined in section 4. When plotting profiles of variables along the transverse direction z, the wall is marked by a grey field to better visualize the fluid-solid interface.

5.1. Main characteristics of the investigated flow

The main features of the studied magneto-convective flow for *Case 1* (see table 1) are briefly described by considering time-averaged quantities in order to better explain the problem that we are dealing with. The full characterization of the flow also in terms of time-dependent phenomena will be derived in the section dedicated to the comparison of results obtained by different codes.

In figure 2 contours of time-averaged temperature are plotted on the fluid-wall interface at $y = z{=}-0.023$ m. For better visualization of the velocity distribution and electric currents (shown in figure 3), the channel is displayed so that the gravitational field **g** is horizontal. The region on which the surface heat flux q'' is applied is marked by red arrows and clearly visible on the plane $z = -0.023$ m, which is aligned with the magnetic field and named side or parallel wall. Here contours of temperature are shown. On the wall perpendicular to the imposed magnetic field, called Hartmann wall, it can be seen how the thermal layer grows when moving downstream.

Table 4. Boundary conditions (BCs) at inlet and outlet of the computational domain. FDF indicates the fully developed hydrodynamic profile (viscous laminar or turbulent), (*) for Case 2 artificial high viscosity in last 0.2 m, (**) backflow allowed at exit. Missing BCs could not be provided by users.

Code	Inlet	Outlet	Duct length (m)
FLUENT CIEMAT	FDF laminar $\partial_x p = 0$ $\partial_x \phi = 0$ $T = 300\ ^\circ$C	u */** $p = 0$ $\partial_x \phi = 0$ $\partial_x T = 0$	2.2 (*Case 1*) 2.3 (*Case 2*)
FLUENT UK	$\partial_x u = 0$ $p = 0$ $\partial_x \phi = 0$ $T = 300\ ^\circ$C	$\dot{m} = \text{const}$ $\partial_x \phi = 0$	3
CFX	$u = \text{const}$ $\partial_x \phi = 0$ $T = 300\ ^\circ$C	u: opening ** $p_{\text{mean}} = 0$ $\partial_x \phi = 0$ $T = T_{\text{bout}}$ (energy balance)	2 .25
OF ORNL	$u = \text{const}$ $\partial_x p = 0$ $\partial_x \phi = 0$ $T = 300\ ^\circ$C	$\partial_x u = 0$ * $p = 0$ $\partial_x \phi = 0$ $\partial_x T = 0$	2.0 (*Case 1*) 2.3 (*Case 2*)
OF KIT	FDF turbulent $\partial_x p = 0$ $\phi = 0$ $T = 300\ ^\circ$C	$\partial_t u + u\partial_x u = 0$ $p = 0$ $\phi = 0$ $\partial_x T = 0$	3
COMSOL	$u = \text{const}$ $\partial_x \phi = 0$ $T = 300\ ^\circ$C	$\partial_x u = 0$ $p = 0$ $\partial_x \phi = 0$ $\partial_x T = 0$	2.5

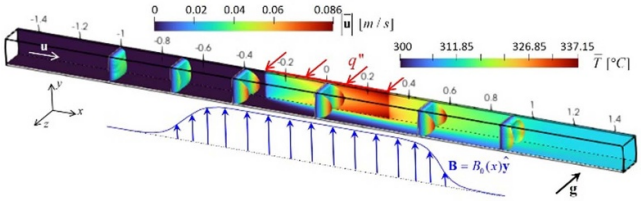

Figure 2. Results for the flow at $Ha = 235$ ($B_0 = 0.5$ T), $Gr = 1.42{\cdot}10^7$ ($q'' = 4$ W cm^{-2}), $Re = 3220$ ($u_0 = 0.03$ m s^{-1}) (*Case 1*). Contours of time-averaged temperature are plotted on the fluid-wall interfaces at $z = -0.023$ m and $y = -0.023$ m. Profiles of velocity are displayed on various cross-sectional planes. The distribution of the magnetic field is sketched below the figure and the imposed surface heat flux q'' is marked by red arrows.

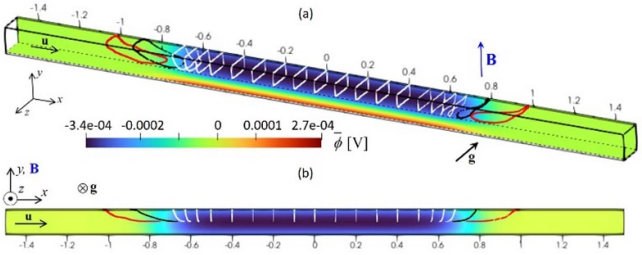

Figure 3. Results for the flow at $Ha = 235$, $Gr = 1.42{\cdot}10^7$ and $Re = 3220$ (*Case 1*). Contours of electric potential on the external surface of the wall at $z = -0.025$ m and on the fluid-wall interface $y = -0.023$ m. Electric current loops are plotted only in half of the duct for $y > 0$ for better visualization.

Velocity profiles are displayed at various axial positions and colored by the magnitude of the time-averaged velocity. When the incoming hydrodynamic flow enters the magnetic field ($x = -1$ m), induced electromagnetic Lorentz forces brake the flow in the duct core and lead to the formation of the so-called M-shaped MHD velocity profiles, as typical in electrically conducting ducts. The latter is characterized by a uniform core and increased velocity in the boundary layers along the parallel walls. By approaching the exit of the magnet, the electromagnetic forces become weaker and they cannot sustain any longer the high velocity jets in the boundary regions that gradually disappear.

The motion of the electrically conducting PbLi in the imposed magnetic field induces electric currents in the liquid metal. In figure 3, current loops are plotted showing that in the central part of the duct, where the magnetic field is constant ($|x| < 0.4$ m), the current induced in the fluid closes through the wall moving preferentially in cross-sectional yz planes. At the entrance and exit of the magnet, gradients of electric potential arise, as visible on the planes $y = -0.023$ m and $z = -0.025$ m

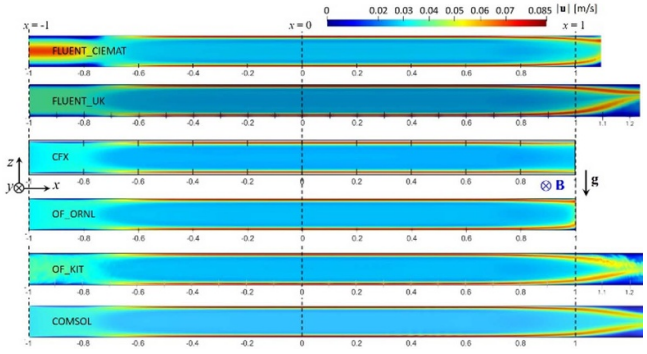

Figure 4. Contours of instantaneous velocity on the plane $y = 0$.

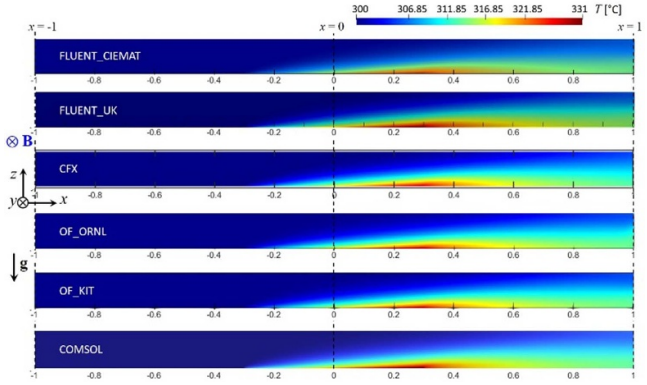

Figure 5. Contours of instantaneous temperature on the plane $y = 0$.

where contours of time-averaged potential are displayed. The axial component of potential gradient drives axial electric currents that lead to the formation of 3D paths (e.g. black and red lines). The xy view in figure 3(b) shows well the transition 3D($x < -0.4$ m) $\rightarrow$ 2D($|x| < 0.4$ m) $\rightarrow$ 3D($x > 0.4$ m) in the current distribution along the x direction with the progressive formation of an axial current component in regions of fringing magnetic field.

5.2. *Code-to–code comparison: case 1*

In the following, the characteristics of the flow of *Case 1* are presented through the comparison of data obtained with the different codes. In this case, the relatively high velocity of the forced flow and the low value of the applied surface heat flux does not result in appreciable mixed convection effects and the flow retains mostly an isothermal-like MHD character.

In figure 4 contours of instantaneous velocity are plotted on the middle plane $y = 0$ perpendicular to the magnetic field. It should be mentioned that, in order to permit a reasonable visualization of the long computational domain, the cross-section of the geometry has been scaled by a factor 2.5 in y and z direction. For simulations that use a longer computational domain, an additional portion of the exit part of the duct is shown in order to appreciate the transition from MHD to hydrodynamic flow. The expected formation of two high-velocity jets in the boundary layers along the side walls and the reduction of the velocity in the middle of the duct is clearly visible when the flow enters the magnetic field (cf figure 2). In the middle section of the duct a good agreement is found among results obtained by different codes, while those in the inlet and outlet parts exhibit some variation depending on the boundary conditions used. Data from FLUENT_UK present a smaller core velocity.

Contours of instantaneous temperature on the plane $y = 0$ are displayed in figure 5. The development of the thermal layer is well predicted by all the codes. The temperature distribution develops slowly in the channel. The flow maintains a laminar regime under the influence of the electromagnetic forces that reduce the heat transfer intensity. Buoyancy forces are weak and do not lead to any significant mixing. Close to $x = 1$ m, a residual thermal stratification is still present in the

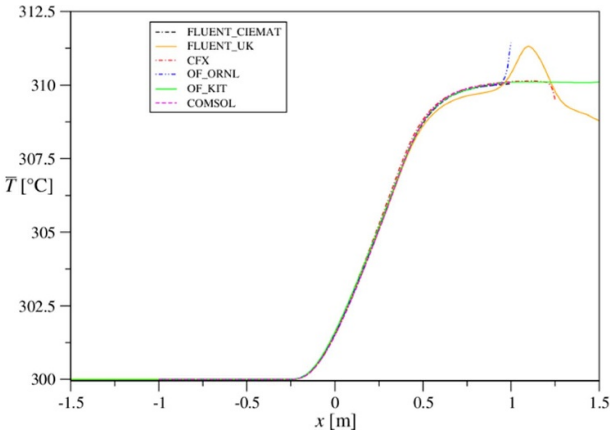

Figure 6. Time-averaged temperature along the axis of the duct at $y = z = 0$.

fluid between the upper ($z > 0$) and lower ($z < 0$) halves of the duct.

The time-averaged temperature is plotted in figure 6 along the duct axis at $y = z = 0$. Results fit well together apart at the outlet due to different exit conditions and lengths of the computational domain (table 4). The only data that deviates significantly from the others (orange line) is probably a result of a not fully converged solution and, as a consequence, a too short range of time to obtain statistically converged time-averaged data. In a large portion of the computational domain (-0.75 m $< x < 0.8$ m), the results exhibit a good agreement.

In figure 7 the time-averaged axial velocity is plotted as a function of the coordinate x. The central velocity initially grows, attempting to reach the value expected in a fully established hydrodynamic flow. At $x \approx -0.85$ m the velocity starts decreasing due to the occurrence of significant electromagnetic forces. Simultaneously the velocity in the parallel layers begins increasing leading to the formation of the MHD M-shaped profile (see figure 2). The core velocity remains almost constant for -0.4 m $< x < 0.6$ m. In the outlet section, the maximum velocity shifts progressively towards the center of the duct, while approaching a time-dependent hydrodynamic regime.

The axial distribution of the time-averaged pressure is displayed in figure 8 along the axis of the channel for $y = z = 0$.

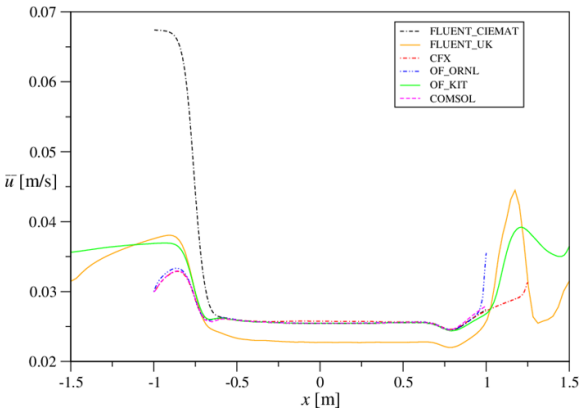

Figure 7. Time-averaged axial velocity along the axis of the duct at $y = z = 0$.

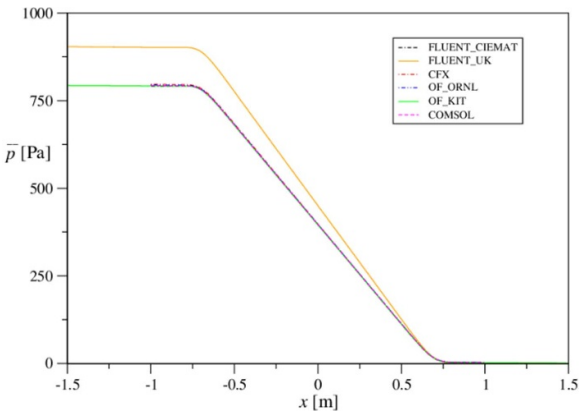

Figure 8. Time-averaged pressure along the axis of the channel at $y = z = 0$.

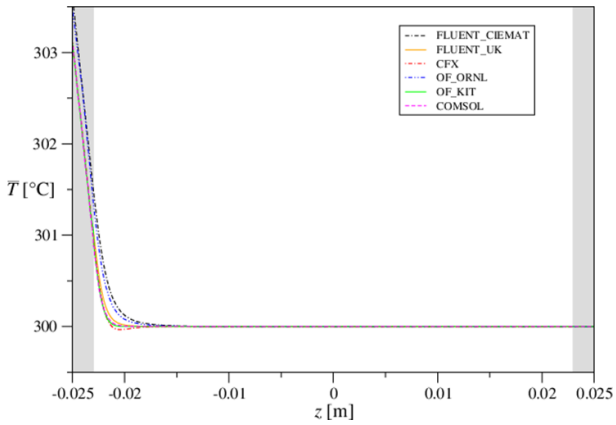

Figure 9. Time-averaged temperature plotted along the transverse direction z, at $y = 0$ and $x = -0.3$ m.

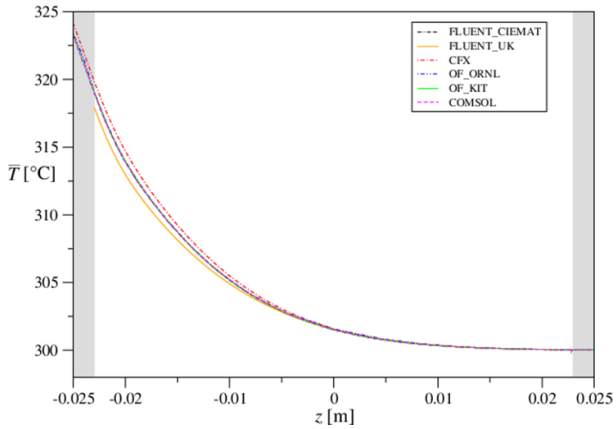

Figure 10. Time-averaged temperature plotted along the transverse direction z, at $y = 0$ and $x = 0$.

The hydrodynamic pressure gradient at the entrance and exit is negligible compared to the one in the magnet. Here, when the magnetic field becomes constant, the pressure varies linearly indicating that the flow reaches fully developed conditions. The uniform pressure gradient, $\partial p/\partial x = -0.0855$, fits well with the one predicted by the analytical solution for a fully developed isothermal MHD flow in a duct with electrically conducting walls, $\partial p/\partial x|_{\mathrm{FDF}} = -0.0863$, despite the presence of buoyant forces for $|x| < 0.3$m. All simulations show quite good agreement apart from those of FLUENT_UK, indicating the shortcoming of the latter simulation. The reason of such discrepancy with the other data cannot be explained by the code itself, since results from FLUENT_CIEMAT well reproduce the flow features.

Let us consider now the distribution of the temperature along the transverse direction z at different axial positions in order to understand how the thermal layer develops when the flow moves downstream along the heated wall. In figure 9, $\bar{T}(y = 0, z)$ is plotted at $x = -0.3$ m where the heating on the external surface starts. The thin thermal layer at this position is due to the conjugate heat flux in the wall. In a large part of the duct cross-section, the temperature is still equal to the entrance value of 300 °C. The deviation of the OF_ORNL and FLUENT_CIEMAT results derive probably from the insufficient resolution in axial direction that is lower than for the other simulations (see table 3).

When the fluid moves downstream, the liquid metal warms up and the thickness of the thermal layer increases, as visible in figure 10, in which the time-averaged temperature is plotted in the middle of the heated zone at $x = 0$. The development of the thermal layer can be seen also by considering profiles at various axial positions as displayed in figure 11. By moving downstream, the temperature at the fluid-wall interface increases and the layer becomes thicker. When the heat flux at the external wall ends at $x = 0.3$m, the temperature at the liquid metal-solid interface starts reducing and the temperature distribution across the channel height becomes more homogeneous. The temperature on the opposite side wall at $z = 0.023$ m starts increasing at about $x = 0$ and becomes larger and larger. Grid sensitivity studies highlighted the significant influence of the axial resolution on the temperature distribution especially near $x = -0.3$ m, where the heat is first applied, and at the exit of the magnet where small time-dependent structures appear.

In figures 12 and 13 the distribution of time-averaged axial velocity is plotted along the transverse z direction, on the middle plane at $y = 0$, at two axial positions, $x = -0.3$ m

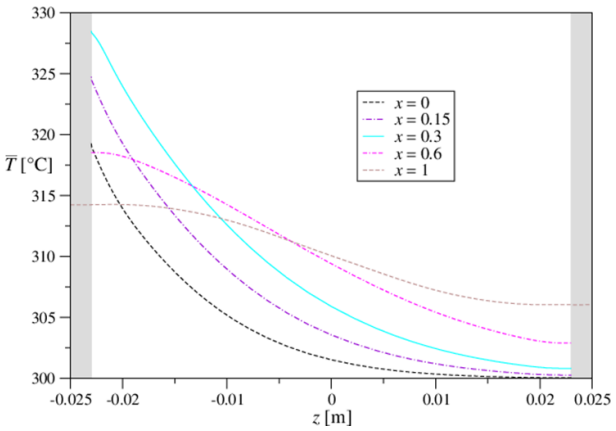

Figure 11. Time-averaged temperature in the fluid plotted along the transverse coordinate z, at $y = 0$ and various axial positions (OF_KIT). The curves for $x = 0$ and $x = 1$ m are the same as shown in figures 10 and 11. In the legend the coordinate x is given in meters.

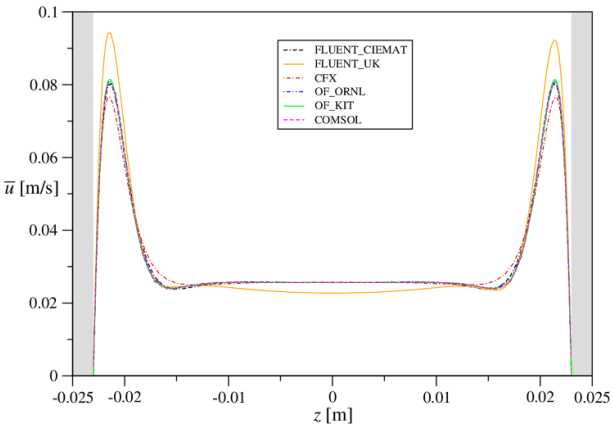

Figure 12. Time-averaged axial velocity along the z coordinate at $y = 0$ and $x = -0.3$ m.

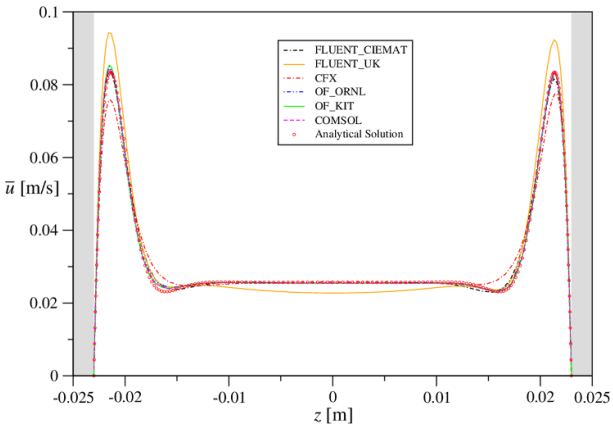

Figure 13. Time-averaged axial velocity along z at $y = 0$ and $x = 0$.

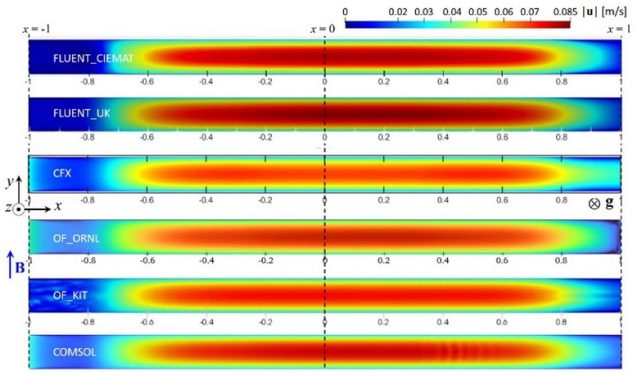

Figure 14. Contours of instantaneous velocity on the plane $z = 0.022$ m indicating the jet in the parallel layer.

and $x = 0$. The velocity profile is characterized by a uniform core and high-velocity jets in the layers along walls parallel to the magnetic field, as expected for isothermal MHD flows in electrically conducting ducts. In the center of the heated zone at $x = 0$ (figure 13) the only effect of convection is a slight asymmetry of the velocity profile. Most of the codes that yield accurate results predict a minimally increased maximum velocity in the jet close to the heated wall ($z = -0.023$ m). The red symbols indicate the analytical solution that agrees pretty well with results obtained by FLUENT_CIEMAT, OF_KIT, OF_ORNL and COMSOL. Two sets of data deviate from the analytical solution. For FLUENT_UK an explanation could be a lack of convergence of the solution. This conclusion is supported also by the comparison of other quantities. In case of CFX, the reason could be related to numerical diffusion rather than inadequate mesh density or too short computational time, since most of the flow features are accurately predicted by this code. Up to about $x = 0.5$ m the velocity profiles resemble the analytical solution as in figure 13. Further downstream, while the strength of the magnetic field becomes smaller, the maximum velocity reduces and the thickness of the parallel layers increases, since the velocity profile evolves towards a hydrodynamic distribution.

The transition from hydrodynamic to MHD conditions with the rise of the velocity in the side layer is visible in figure 14 where contours of instantaneous velocity are plotted on the plane at $z = 0.022$ m close to the side wall. Results obtained by OF_KIT show the unstable flow at the entrance and exit of the magnet. For $|x| < 0.4$ m, the Lorentz force is dominant since the field has reached its maximum value B_0. The flow in the core region retains an almost uniform value until $x = 0.6$ m. Results in figures 4 and 14 confirm previous observations according to which buoyancy forces in *Case 1* do not significantly modify the flow compared with an isothermal MHD flow.

As observed at the beginning of this section, when describing the main general features of the magneto-convective flow under study, due to the spatial variation of the magnetic field, axial gradients of the electric potential $\partial\phi/\partial x \neq 0$ arise for $|x| > 0.45$ m till the magnetic field vanishes. The axial distribution of the time-averaged ϕ is displayed in figure 15 along the warm side wall at $z = -0.023$ m. On the opposite parallel wall at $z = 0.023$ m the potential distribution is almost the same, apart from the reversed sign, with very small deviations where the heat is applied to the external surface. Hence, the

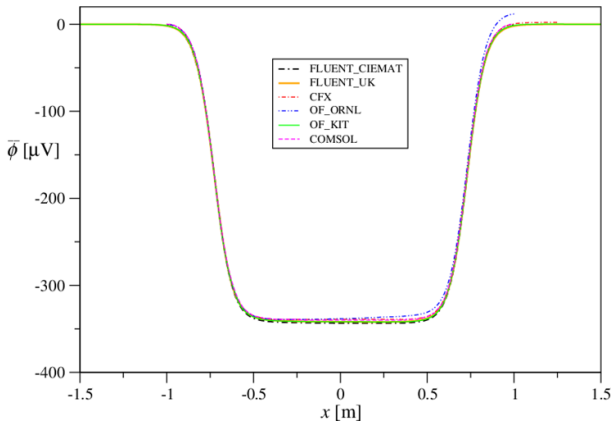

Figure 15. Time-averaged electric potential along the axial coordinate x at $y = 0$, at the side wall at $z = -0.023$.

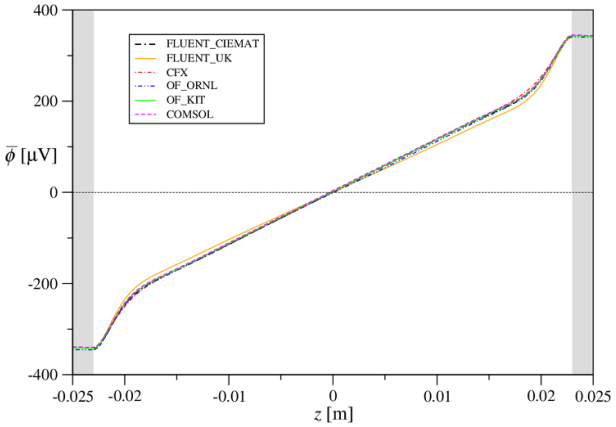

Figure 16. Time-averaged electric potential along the transverse coordinate z, at $x,y = 0$.

total transverse potential difference $\phi(x,y = 0, z = 0.023\ \text{m})$—$\phi(x,y = 0, z = -0.023\ \text{m})$ that establishes between the side walls has an analogous distribution as the curve in figure 15 with a nearly double maximum value. The latter remains constant in the region of uniform magnetic field, where the flow is almost fully established (compare figures 7 and 8). Most of the data fits well together.

The transverse profile of the electric potential in the middle of the duct ($x = y = 0$) is plotted in figure 16 showing the expected MHD distribution with a linear profile in the core and non-linear contribution close to the walls. While most of the data agree quite well, slight deviation is observed for FLUENT_UK, as in previous figures.

As a measure of the average temperature in the duct, we calculate the mean bulk temperature according to

$$\bar{T}_b(x) = \frac{\int_A \bar{u}\bar{T}\mathrm{d}A}{\int_A \bar{u}\mathrm{d}A}. \tag{6}$$

In figure 17, the bulk temperature is plotted along the axial coordinate x. In the region in which the constant surface heat flux is applied, $\bar{T}_b$ increases linearly from the inlet temperature $T_\mathrm{i} = 300\ ^\circ\mathrm{C}$ to the exit value of about $T_\mathrm{e} = 310\ ^\circ\mathrm{C}$.

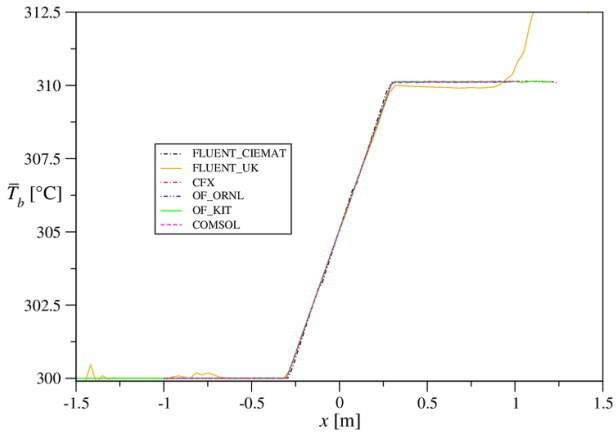

Figure 17. Bulk temperature T_b along the coordinate x.

Discrepancies and non-physical behavior are observable in the FLUENT_UK data probably due to both a not fully converged solution and issues at the outlet owing to the applied boundary conditions.

The convective heat transfer in the flow can be quantified by defining a heat transfer coefficient h and a Nusselt number Nu, which gives a non-dimensional measure for the intensity of the convective heat transport close to the heated wall:

$$\begin{aligned} h &= q''/\left(\bar{T}_w(x, y = 0, z = -0.023) - \bar{T}_b(x)\right), \\ Nu &= h\frac{L}{k}, \end{aligned} \tag{7}$$

where q'' is the imposed surface heat flux, $\bar{T}_\mathrm{w}$ is the time-averaged temperature at the fluid-wall interface on the middle plane of the duct ($y = 0$, $z = -0.023$ m) and $\bar{T}_b(x)$ is the bulk temperature defined by equation (6).

In figure 18 the Nusselt number Nu is plotted along the axial coordinate x. At $x = -0.3$ m, at the beginning of the heated zone, the bulk temperature and the one at the fluid-wall interface start increasing, the latter much faster than the former one (as shown later in figure 38). The growth rate of the wall temperature reduces by moving downstream. The convective heat transport close to the side wall is larger than in the duct center due to the presence of the high-velocity jets in the boundary layer (see e.g. figure 12). It can be observed that when approaching $x = 0.3$m the Nusselt number tends to an asymptotic value $Nu \to 2.45$, indicating that the flow may near a fully developed state at the end of the heated section.

Due to the presence of buoyancy forces a secondary flow in the transverse yz direction occurs. In order to better characterize the flow regime in terms of flow mixing and to understand the impact on the main flow of the onset of the secondary flow, the normalized mean kinetic energy of the latter one is calculated. It quantifies the transverse circulation and is defined according to [19] as

$$\bar{E}_t(x) = \frac{1}{Au_0^2}\int \left(\bar{u}_y^2 + \bar{u}_z^2\right)\mathrm{d}A. \tag{8}$$

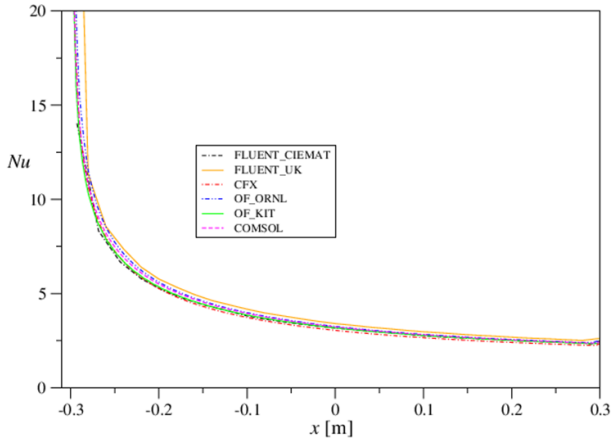

Figure 18. Nusselt number, defined according to equation (7), plotted along the axial coordinate x.

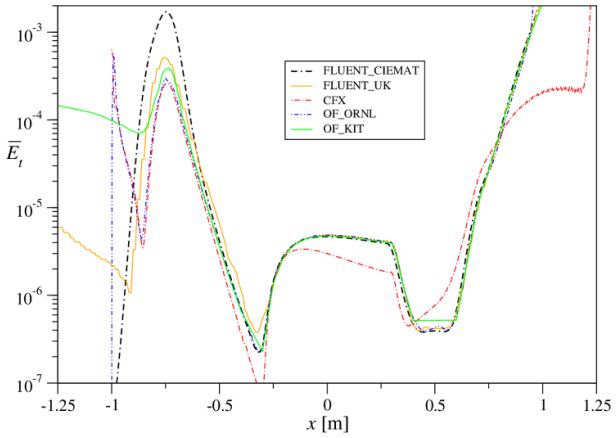

Figure 19. Kinetic energy $\bar{E}_t$ of the transverse flow (u_y, u_z) plotted along the axial coordinate x. COMSOL data is not shown due to large discrepancy caused by problems in the evaluation of equation (8).

In equation (8), A is the area of the duct cross-section, $\bar{u}_y$ and $\bar{u}_z$ are the time-averaged velocity components in a plane perpendicular to the main axial stream. The mean velocity u_0 is used to scale the velocity.

In figure 19 the mean normalized transverse kinetic energy $\bar{E}_t$ is plotted along the axial coordinate. Within the uniform region of the magnetic field, when $B(x) \approx B_0$, the transverse flow and its kinetic energy are very small, which confirms the weak effects of the buoyant forces. The transverse kinetic energy, which starts increasing at the edge of the heated region, reaches a maximum and then decreases monotonically till $x = 0.3$m where the surface heat flux vanishes. In the center of the duct, at $x = 0$, a very weak transverse circulation with velocity of the order of 10^{-4} m s^{-1} caused by convection can be identified, which is characterized by two counter-rotating cells, as shown in figure 20 (left) by white streamlines together with contours of the magnitude of the transverse velocity $\mathbf{u}_t$. The normalized kinetic energy of the recirculation in this plane is of the order of 10^{-6}. This type of additional circulation, whose rotation axis is perpendicular to the imposed magnetic field, tends to be suppressed by the electromagnetic forces. A detailed description of this secondary motion for different flow parameters can be found in [19] for a channel with electrically insulating walls and a uniform imposed magnetic field. This transverse recirculation does not significantly affect the streamwise velocity profile, which resembles the one of an isothermal MHD flow, as already observed.

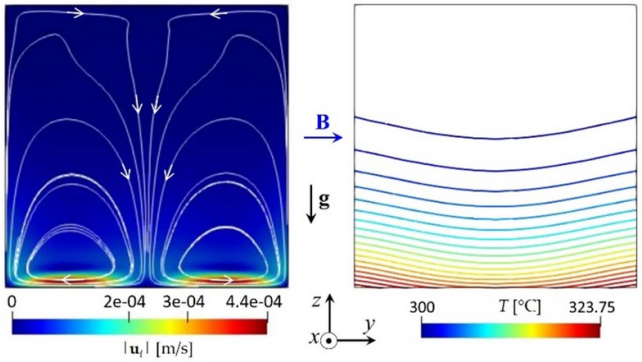

Figure 20. (Left) Contours and streamlines of transverse plane circulation $\mathbf{u}_t$, and (right) contours of temperature on the cross-sectional plane $x = 0$ (OF-KIT).

At the entry and exit of the magnet, at $|x| \approx 0.75$ m, all codes show increased transverse motion, caused by 3D effects in the fringing magnetic field, where the flow is pushed by strong Lorentz forces towards the parallel layers and to the middle of the duct, respectively. The rapid increase in transverse flow close to $x = -1$ m is apparently an artifact caused by entrance conditions and by the finite length of the simulation domain, which starts at $x = -1$ m for most of the calculations. When the computational domain is extended upstream, this singular behavior at $x = -1$ m is not present as can be seen from the OF_KIT and FLUENT_UK results, where the intensity of the hydrodynamic turbulent entry flow is first damped by the increasing magnetic field, before the strong 3D MHD effects reshape the flow near $x \approx -0.75$ m, as observed above. Similar unphysical artifacts are observed also at the exit of the duct, in those simulations where a backflow occurs near the outlet.

Figure 20 on the right shows temperature contours plotted on the plane $x = 0$. The reduced temperature in the center of the heated wall results from an increased heat transfer due to the parabolic shape of the jet in the parallel layer (see figure 2), but may also be partly caused by the weak secondary transverse convective transport.

Conclusions for case 1

Considering the results presented in figures 4–20, it can be concluded that the main flow features of *Case 1* are well predicted by almost all the codes.

There are some notable differences in the results obtained by FLUENT_UK. Figures 8 and 12 show that the predicted pressure gradient and the velocity profile in a cross section

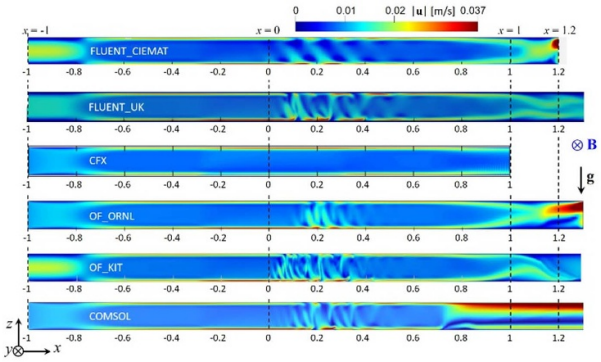

Figure 21. Contours of instantaneous velocity on the plane $y = 0$.

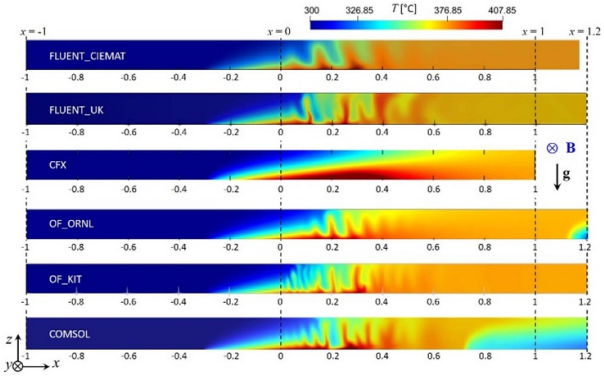

Figure 22. Contours of instantaneous temperature on the plane $y = 0$.

where the flow is almost fully developed do not agree with other code predictions and with the analytical solution. The deficiencies observed in the FLUENT_UK simulations, since the computational domain appears to be well resolved by the grid used, as shown in table 3, could be ascribed to a too short computational time and the need to check more accurately the convergence of the solution. As a consequence, also the time interval on which the time-averaging is performed could be too small.

Grid independence tests showed that the number of grid points in axial direction plays a decisive role in the proper prediction of the thickness of the thermal layer at the beginning of the heated region (cf figure 9).

5.3. Code-to-code comparison: case 2

In this section, we compare the results obtained for *Case 2* (see table 1) in which the Grashof number has been increased and the Reynolds number reduced compared to *Case 1*. Important features of the flow can be seen by considering contour plots of instantaneous velocity and temperature on the middle plane of the duct at $y = 0$, as shown in figures 21 and 22, respectively. As a result of the scaling of the cross-section by a factor 2.5, perturbations look more elongated along z and narrower in axial direction than in the unscaled contour plot. However, flow characteristics remain unchanged. Simulations with higher axial resolution (see table 3) reveal, as expected, more details of the time-dependent flow.

Most of the simulations predict reasonably well the major physical phenomena that characterize the flow at the entrance of the magnet and of the heated zone. Remarkable differences can be observed in CFX data, which predicts a stationary flow. Significant perturbations in the stream are clearly visible for $0 < x < 0.45$ m. The outcome from COMSOL clearly evidence issues in the outlet boundary conditions and the occurrence of a backflow. In general the comparison suggests that the quality of time-averaging is different among the codes and that the selection of the time-averaging interval can significantly affect the data. Table 5 summarizes the time intervals used by each code for calculating the time-averaged results in *Case 2*. The averaging starts after the simulation reaches a steady state or statistical convergence, so that the average is not influenced by initial transient effects.

Table 5. Time-averaging intervals used by the different codes.

Code	Time-averaging interval (s)
FLUENT_CIEMAT	60
FLUENT_UK	50
CFX	225
OF_ORNL	100
OF_KIT	450
COMSOL	50

In figures 23 and 24 the time-averaged axial velocity and temperature are plotted as a function of the coordinate x along the central line of the duct at $y = z = 0$. CFX results show a different velocity profile in the heated zone and a steeper increase in temperature along the axis compared to other simulations. The strong axial fluctuations of time-averaged results from OF_ORNL could be caused by numerical problems as confirmed also by data in figure 28. This non-monotonic behavior might be related to the finite-difference scheme, computational parameters, as well as to a relatively short time-averaging interval, compared for instance to OF_KIT. Other codes do not suggest that level of fluctuations, even with a shorter time-averaging slot, but they could be more dissipative. Two codes, FLUENT_UK and OF_KIT, predict a clear local maximum in the time-averaged velocity and temperature in the range $0.075\ \text{m} < x < 0.09\ \text{m}$. At this position a very intense exchange of flow between the two side layers occurs and the transverse velocity profile exhibits the strongest asymmetry. This is shown in figure 25 where the time-averaged axial velocity is plotted along the x direction at $y = 0$ and along two lines near the parallel walls at $z = \pm 0.0215$ m. The transverse positions $z = \pm 0.0215$ m correspond to the location of the maximum velocity in the side layers when the flow reaches almost fully developed conditions (see figure 26). The green curve at $z = 0$ is taken from figure 23 and inserted for comparison. It can be noted that the velocity profile remains symmetric in transverse direction till the flow approaches the beginning of the heated wall at $x = -0.3$ m. The maximum value reached by the velocity in the side jets well agrees with the value of the analytical solution (compare figure 26). Behind the end of the warm wall, at $x = 0.33$ m, the velocity in the

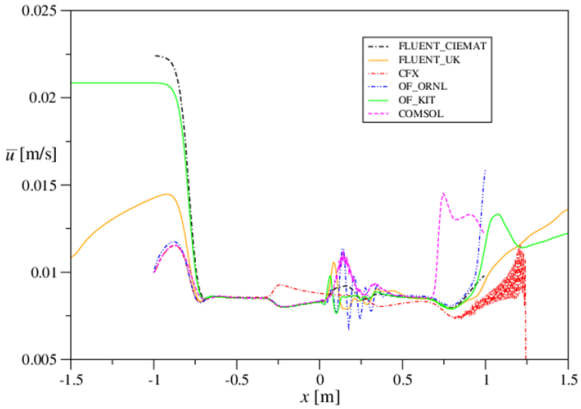

Figure 23. Time-averaged axial velocity along the axis of the duct at $y = z = 0$.

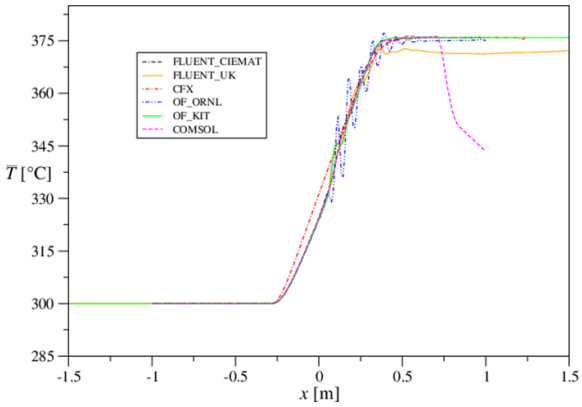

Figure 24. Time-averaged temperature along the axis of the duct at $y = z = 0$.

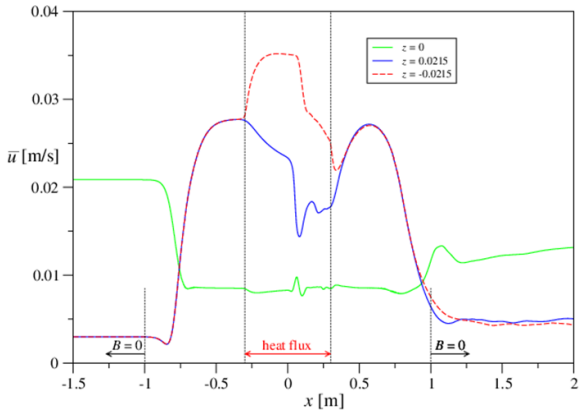

Figure 25. Time-averaged axial velocity (OF_KIT) along the axis of the duct at $y = 0$ and at $z = \pm 0.0215$ m. The green curve (at $z = 0$) is inserted for comparison from figure 23.

side layer at $z = -0.0215$ m (red dashed line) has a local minimum. This indicates the tendency for detachment of the boundary layer from the wall and the ascending motion of the high-temperature fluid towards the upper cold wall.

The symmetric fully developed velocity profile is shown in figure 26 where the time-averaged velocity is plotted along the transverse z coordinate at $x = -0.3$ m. Apart from the solution

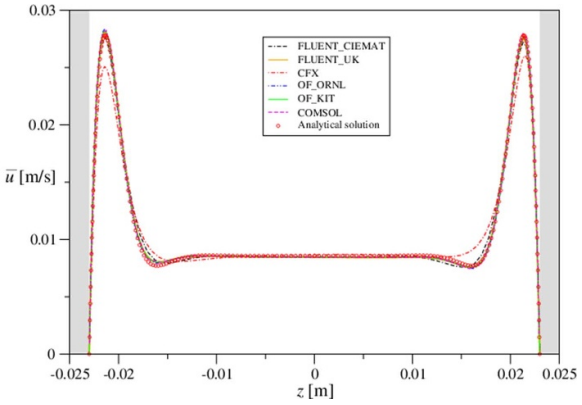

Figure 26. Time-averaged axial velocity along the z coordinate at $x = -0.3$ m and $y = 0$.

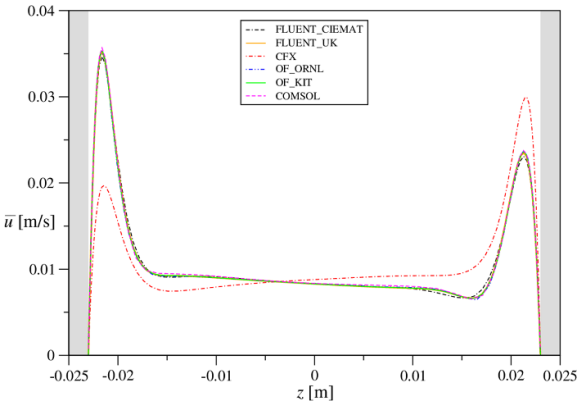

Figure 27. Time-averaged axial velocity along the z coordinate at $x = 0$ and $y = 0$.

calculated by CFX, the other results reproduce in a good way the analytical solution (symbols). The beginning of the heating at the wall is evidenced by the slight asymmetry of the velocity profile. Further downstream, the occurrence of instabilities leads to a stronger asymmetry in the velocity distribution in z direction, as displayed in figure 27 at $x = 0$. Buoyancy forces favor a more intense circulation closer to the lower side of the channel. Perturbations of the axial velocity occur in form of rolls with the axis aligned with the magnetic field.

In order to better understand the characteristics of the flow and to further check how the different codes predict its time-dependent features, temperature, electric potential and pressure are compared at various locations. Figures 28 and 29 illustrate the development of the thermal boundary layer in the duct.

At $x = -0.3$m (figure 28), where the surface heat flux starts, the thermal layer begins to form. Data from COMSOL and OF_KIT fits well together, while most of the other solutions exhibit some deviations. Temperature values obtained by FLUENT_CIEMAT seem too large probably owing to a poor axial resolution, while results predicted by OF_ORNL show unphysical oscillations in the wall and in the fluid.

In the middle of the heated region at $x = 0$ all the codes predict properly the thicker thermal layer as shown in figure 29.

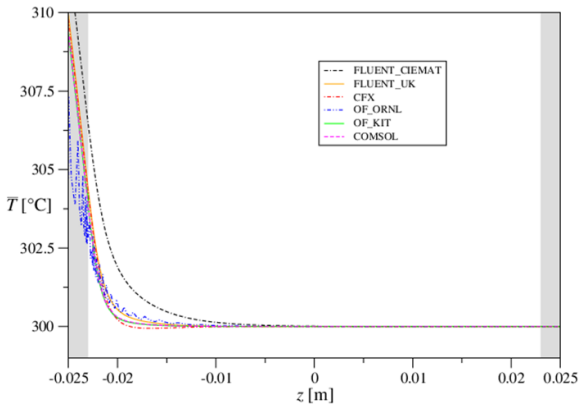

Figure 28. Time-averaged temperature plotted along the transverse direction z, at $y = 0$ and x=−0.3m.

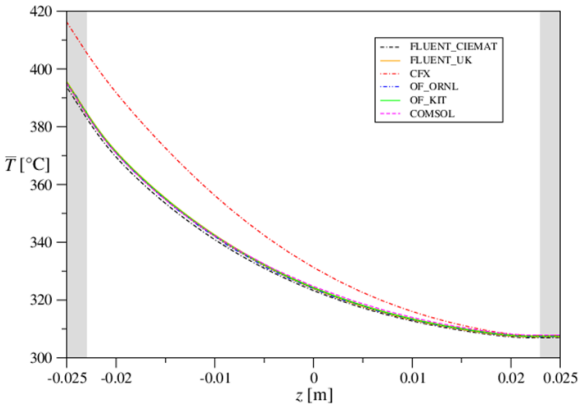

Figure 29. Time-averaged temperature plotted along the transverse direction z, at $y = 0$ and $x = 0$.

Close to the end of the heated region at $x = 0.33$ m the boundary layer detaches from the heated wall transporting the warm fluid to the upper side wall. By moving downstream, for $x > 0.45$ m, due to the intense mixing caused by velocity perturbations and secondary flow in transverse direction, the temperature difference between top and bottom of the duct reduces and the temperature attains rapidly a uniform distribution (see figure 22). No residual stratification is observed, as present instead in *Case 1* (figure 5).

The increased heat flux on the wall does not significantly affect the distribution of the time-averaged pressure, as shown in figure 30, where $\bar{p}$ is plotted along the middle line of the duct. Instead, buoyancy forces have a noticeable impact on the electric potential distribution. In figures 31 and 32, the electric potential is plotted in the middle of the side walls ($y = 0$) at $z = \pm 0.023$ m. Oscillations present in the curves obtained by FLUENT are due to the fact that they show instantaneous potential, since this time-averaged quantity was not available from the calculations. Along the heated portion of the wall (figure 31) the potential magnitude is locally increased, whereas on the opposite side wall (figure 32) it is slightly reduced. In general, the agreement between simulations seems acceptable.

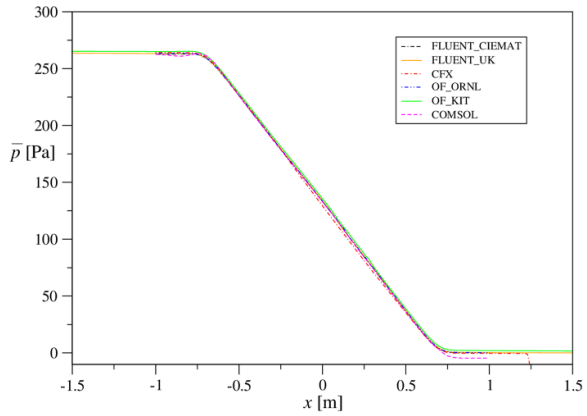

Figure 30. Time-averaged pressure along the axis of the channel at $y = z = 0$. Data from FLUENT_CIEMAT and CFX exhibited an offset that has been removed.

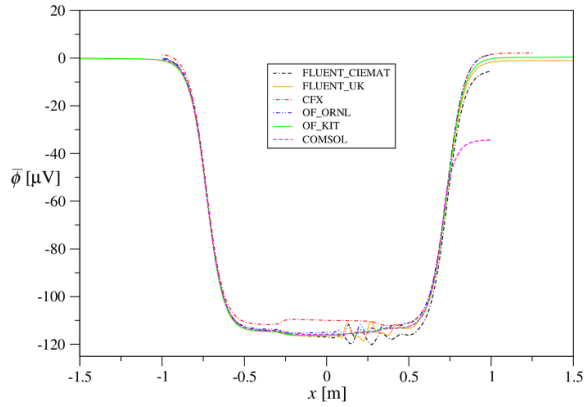

Figure 31. Time-averaged electric potential along the axial coordinate x at $y = 0$, at the side wall at $z = -0.023$ m.

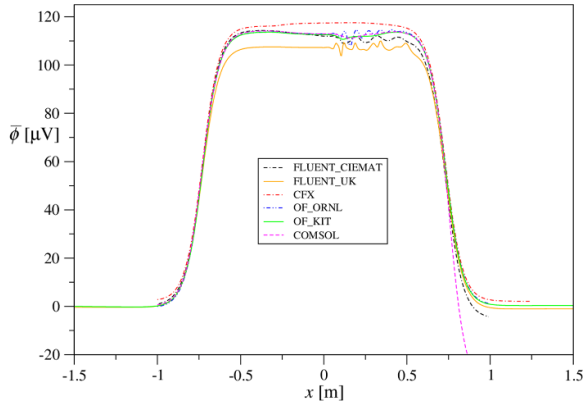

Figure 32. Time-averaged electric potential along the axial coordinate x at $y = 0$, at the side wall at $z = 0.023$ m.

Results obtained by COMSOL have been offset-corrected by defining the reference potential in the center of the inlet. However, it should be noted that, even if this offset seems related to the unclear definition of the potential reference point, it is remarkable that this does not happen for *Case 1*. Deviations close to the exit of the duct are due to the already observed issues with the outlet boundary conditions.

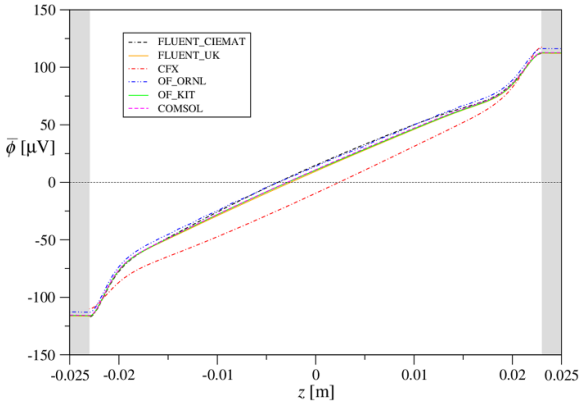

Figure 33. Time-averaged electric potential along the transverse coordinate z, at $x,y = 0$.

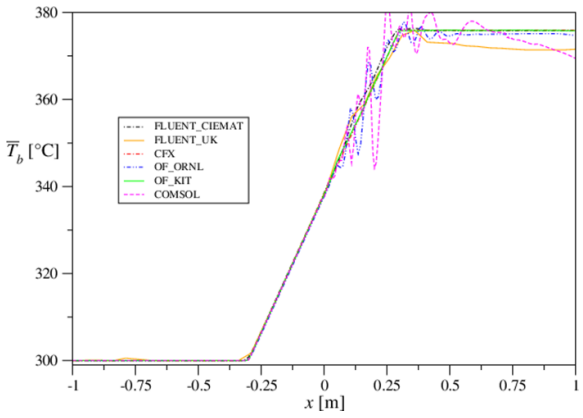

Figure 34. Bulk temperature $\bar{T}_b$ along the coordinate x. OF_ORNL and COMSOL predict unphysical fluctuations.

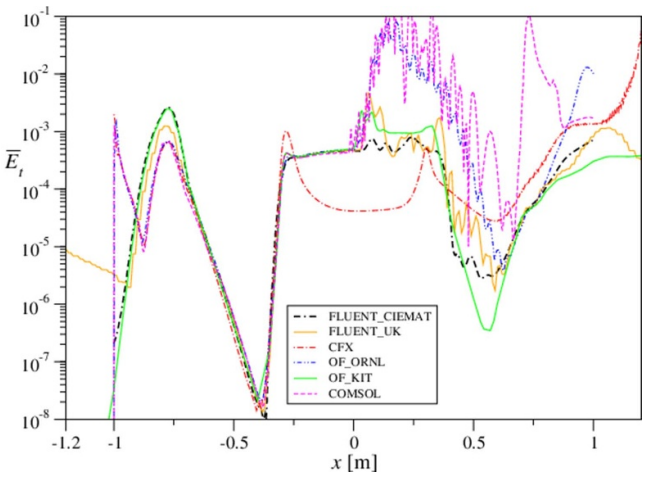

Figure 35. Kinetic energy $\bar{E}_t$ of the transverse flow (u_y, u_z) plotted along the axial coordinate x.

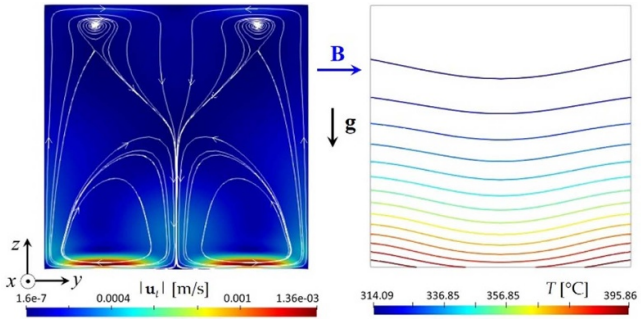

Figure 36. (Left) Contours of transverse plane circulation u_t and streamlines, and (right) contours of temperature on the cross-sectional plane $x = 0.015$ m (OF_KIT).

In figure 33 the time-averaged electric potential is plotted along the transverse coordinate z in the middle of the duct at $x,y = 0$. A good agreement is found among the codes. The profile $\phi(z)$ resembles the one in a fully established flow up to $x = -0.3$ m where the heat flux is applied. In the heated region a deviation from this behavior is observed and the strongest deformation of $\phi(z)$ is present at $x = 0.1$ m.

This special axial position is visible also in the distribution of the bulk temperature in figure 34 (see equation (6)). Around this location, most of the codes exhibit a small deviation from the linear distribution.

An explanation for this peculiarity can be found in the axial distribution of the kinetic energy of the transverse flow $\bar{E}_t$ shown in figure 35. At $x = 0.1$ m a sudden rise in $\bar{E}_t$ occurs, indicating a stronger secondary circulation and a change of the structure of the convective cells. For -0.3 m $< x < 0$, the latter feature two counter-rotating rolls similar to the ones identified in *Case* 1 (figure 20). However, the velocity of the transverse motion is almost one order of magnitude larger. The highest contribution is given by the velocity component u_z, which creates a wavy streamline path. For $0 < x < 0.016$ m four cells appear in transverse cross sections as shown in figure 36. Further downstream the topology of the secondary flow becomes more complex with a shift of the maximum velocity value to the center of the duct and a noticeable impact on the temperature distribution. A detailed investigation of such a structure is out of the purpose of this paper. However, it is worth to mention that temperature fluctuations are present with magnitude up to 30 degrees. Similar phenomena have been found in [19]. The occurrence of these temperature perturbations could play an important role in fusion blankets, since they may cause strong thermal stresses in the structural material.

In figure 35 it can be observed that $\bar{E}_t$ shows a peak at $x \cong -0.78$ m. This corresponds to the significant relocation of the fluid from the center towards the walls of the duct when the flow enters the magnetic field. This redistribution of the fluid is due to the induction of electromagnetic forces. As a result, the hydrodynamic velocity profile starts becoming flat, the velocity reduces in the core and increases in the side layers (see e.g. figure 21). The MHD flow develops then into a quasi fully developed flow (figure 26) before reaching the heated wall. Here at $x = -0.3$ m the kinetic energy increases again, the transverse velocity profile becomes strongly asymmetric (figure 27) with higher velocity at the heated wall. The largest transverse kinetic energy is found at $x \cong 0.1$ m, where intense perturbations in temperature and velocity occur, as already pointed out. A different behavior is observed in data from

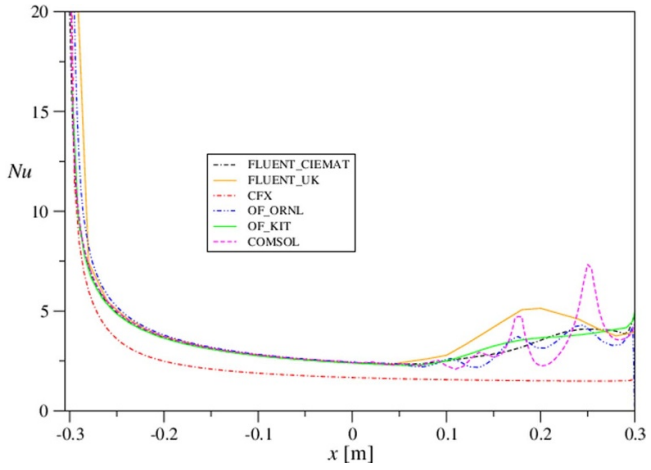

Figure 37. The Nusselt number, defined according to (7), is plotted along the axial coordinate x.

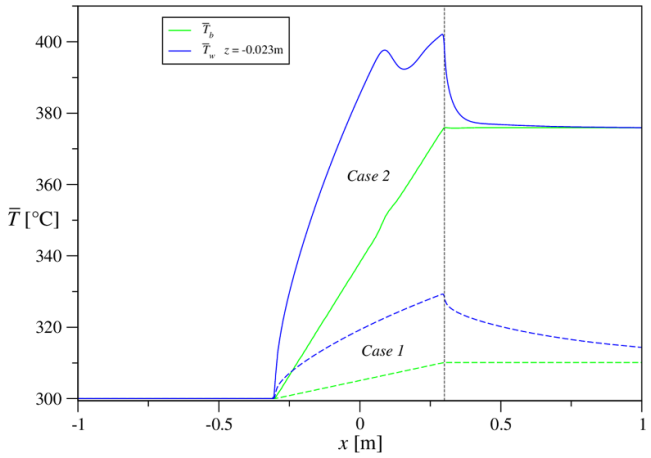

Figure 38. Axial distribution of time-averaged temperature (OF_KIT) at the heated wall ($z = -0.023$) and of bulk temperature for *Case 1* (dash lines) and *Case 2* (solid lines).

CFX. It should be noted that both OF_ORNL and COMSOL predict unphysical fluctuations in the bulk temperature and in the kinetic energy. Such problems could derive from the way in which equation (6) has been evaluated and from the time-averaging of the velocity.

In order to quantify the heat transfer between the heated wall and the liquid metal, the Nusselt number Nu is calculated according to equation (7). In figure 37 Nu is plotted along the axial direction in the heated zone. Compared to *Case 1* (figure 18) the Nusselt number is smaller for $-0.3\ \text{m} \leqslant x \leqslant 0.1\ \text{m}$. The weaker forced flow leads to a smaller convective heat transfer even if the surface heat flux is increased. For $x > 0.1$ m perturbations in velocity and temperature fields as well as a significant secondary motion in transverse direction are present, which enhance the heat transfer in the fluid. It can be observed that the resulting increased mixing contributes to rapidly achieve a convergence between $\overline{T}_\text{w}$ and $\overline{T}_b$ as displayed in figure 38 (solid lines). *Case 1*, in which temperature stratification persists up to the outlet of the duct, is shown for comparison (dash lines).

Conclusions for case 2

The comparison of results for *Case 2* shows that almost all codes can predict the general flow features but important differences occur when large perturbations develop. This is especially evident in the transverse kinetic energy and in the Nusselt number. The chosen outlet boundary condition affects significantly the solution in the last portion of the computational domain. In particular, large non-physical velocity values appear at the outlet. Even the use of artificial high viscosity in an additional extended portion of the channel does not solve this problem. Tests performed by using different lengths of the computational domain and various mesh resolutions in the final part of the duct highlight how a sufficiently long channel and a fine grid significantly help to prevent the occurrence of this unphysical large velocity.

Another important conclusion that can be achieved by considering the data obtained by CFX is the significant impact of numerical diffusion on the solution. In particular, this artificial diffusion, which appears due to the discretization process of the convective terms of the transport equations, has a smoothing effect on flow instabilities.

6. Concluding remarks

In order to further validate codes used for the prediction of MHD flows, as they occur in blankets for fusion reactors, a benchmark project has been started to complement the one described by Smolentsev *et al* [8]. The present comparison of numerical results shows that most simulations were able to predict major physical phenomena in both cases considered. The agreement in the region of the magnetic field remains reasonably good for flows that are stationary and laminar. When flow separation occurs or when the flow becomes time-dependent or turbulent, differences between simulations were revealed. Those deviations may be related to numerical diffusion, insufficient resolution of the computational domain, or averaging over too short time intervals. It has been further observed that entrance and exit conditions affect the results even far away from these boundaries.

The performed code-to-code benchmark highlights the fact that the available codes, both commercial and open-source, can produce reliable data. However, some important user-related choices may strongly affect the results.

General recommendations for rigorous validation of a numerical code have been given e.g. in [20]. The comparison among results from the six research teams, as described in this paper, support the definition of those important benchmark rules. The latter represent also the required steps for an accurate formulation of a code-to-code comparison and they are here summarized:

- general description of physical problem being modeled
- definition of initial and boundary conditions, and any auxiliary needed conditions
- list of
  - o employed numerical algorithms and discretization schemes for each term in the equations

  - o assumptions used to formulate the mathematical model
- description of grid topology and number of points in the computational domain (special requirements for MHD boundary layers [4]).

Different methods are available to check the accuracy of the numerical solution during the run (tolerances have to be properly specified):

- Follow the temporal evolution of:
  - o Residuals for velocity, pressure, temperature and electric potential.
  - o Variable values in monitoring points. The latter should be located in regions where strong gradients are expected. Monitoring data is relevant for checking the establishment of stationary conditions or converged statistics in turbulent flow.

Data to be compared for a code-to-code benchmark should satisfy the following requirements:

- using an optimal mesh resolution resulting from systematic grid independence tests
- convergence of the solution being checked as described in the previous paragraph
- in case of time-dependent flow, a sufficiently long time slot has to be selected for collecting meaningful time-averaged values.

Another important issue that has been raised during the benchmark is related to the definition of exit conditions at the outlet of the duct. Most of the simulations show an unphysical increased velocity at the outlet (see e.g. figures 21 and 23). This artifact seems strictly related to the 'outflow' conditions. Although a careful analysis of the influence of the exit conditions is beyond the scope of this paper, a few comments should be made. An ideal method would permit the outgoing stream and any information carried with it to exit the computational domain without adverse upstream effects, in order to avoid the reflection of a wave into the computational domain. A common workaround for this problem is to employ a longer outlet region, such that vortices generated upstream would be sufficiently dissipated before reaching the exit. Hence, tests for the selection of an optimal length of the domain and resolution of the 'outflow' region are mandatory. They were carried out for simulations performed by OF_KIT showing the drawbacks of this practice: a significantly increased number of mesh points associated with larger computational costs in terms of required memory and CPUs. In case of commercial codes, limitations have been pointed out concerning the proper explanation of the mathematical expressions used as outlet boundary conditions and the lack of flexibility in adapting those conditions to the user needs.

From the point of view of the physical phenomena observed in the investigated flow, the occurrence of temperature fluctuations with magnitude of the order of 30 degrees or even more could be of high relevance in fusion reactor blankets. However, in order to understand possible implications of these perturbations for applications in fusion technology, it is necessary to consider specific blanket concepts with their complex design, presence of volumetric heating, electromagnetic and thermal coupling of adjacent fluid domains, as well as the proper range of parameters.

Acknowledgment

This work has been carried out within the framework of the EUROfusion Consortium, funded by the European Union via the Euratom Research and Training Programme (Grant Agreement No. 101052200—EUROfusion). Views and opinions expressed are however those of the authors only and do not necessarily reflect those of the European Union or the European Commission. Neither the European Union nor the European Commission can be held responsible for them.

This work was partially supported by the computing facilities of Extremadura Research Centre for Advanced Technologies (CETA-CIEMAT), funded by the European Regional Development Fund (ERFD). CETA-CIEMAT belongs to CIEMAT and the Government of Spain.

ORNL acknowledges financial support from US DOE under contract number DE-AC05-00OR22725. The U.S. government retains and the publisher, by accepting the paper for publication, acknowledges that the U.S. government retains a nonexclusive, paid-up, irrevocable, worldwide license to publish or reproduce the published form of this manuscript, or allow others to do so, for U.S. government purposes. DOE will provide public access to these results of federally sponsored research in accordance with the DOE Public Access Plan (www.energy.gov/doe-public-access-plan).

Sapienza University authors acknowledge that the computational resources and the related technical support used for this work have been provided by CRESCO/ENEAGRID High Performance Computing infrastructure and its staff [21]. CRESCO/ENEAGRID High Performance Computing infrastructure is funded by ENEA, the Italian National Agency for New Technologies, Energy and Sustainable Economic Development and by Italian and European research programmes, see www.cresco.enea.it/english for information.

ORCID iDs

Chiara Mistrangelo 0000-0002-7464-9887
Leo Bühler 0000-0001-8555-6283
Sergey Smolentsev 0000-0003-1275-0266
Alessandro Tassone 0000-0003-3356-1720
Guillermo G Fonfría 0009-0007-4700-8674
Yuchen Jiang 0000-0002-8328-0284
Lorenzo Melchiorri 0009-0004-1699-7471
Gerasimos Politis 0009-0007-2749-9955
Daniel Suarez 0000-0002-5174-0100
Fernando R Urgorri 0000-0002-3261-1135

References

[1] Mistrangelo C., Bühler L., Alberghi C., Bassini S., Candido L., Courtessole C., Tassone A., Urgorri F.R. and Zikanov O. 2021 MHD R&D activities for liquid metal blankets *Energies* **14** 6640

[2] Ni M.-J., Munipalli R., Morley N.B., Huang P. and Abdou M.A. 2007 A current density conservative scheme for incompressible MHD flows at a low magnetic Reynolds number. Part I: on a rectangular collocated grid system *J. Comput. Phys.* **227** 174–204

[3] Ni M.-J., Munipalli R., Huang P., Morley N.B. and Abdou M.A. 2007 A current density conservative scheme for incompressible MHD flows at a low magnetic Reynolds number. Part II: on an arbitrary collocated mesh *J. Comput. Phys.* **227** 205–28

[4] Smolentsev S. *et al* 2015 An approach to verification and validation of MHD codes for fusion applications *Fusion Eng. Des.* **100** 65–72

[5] Zikanov O., Belyaev I., Listratov Y., Frick P., Razuvanov N. and Sviridov V. 2021 Mixed convection in pipe and duct flows with strong magnetic fields *Appl. Mech. Rev.* **73** 010801–1–35

[6] Sahu S., Courtessole C., Ranjan A., Bhattacharyay R., Sketchley T. and Smolentsev S. 2020 Thermal convection studies in liquid metal flow inside a horizontal duct under the influence of transverse magnetic field *Phys. Fluids* **32** 067107

[7] Koehly C., Courtessole C. and Bühler L. 2025 MaPLE PbLi loop: a facility for investigating MHD convective flows *Fusion Eng. Des.* **215** 115031

[8] Smolentsev S., Rhodes T., Yan Y., Tassone A., Mistrangelo C., Bühler L. and Urgorri F.R. 2020 Code-to-code comparison for a PbLi mixed-convection MHD flow *Fusion Sci. Technol.* **76** 653–69

[9] Gray D. and Giorgini A. 1976 The validity of the Boussinesq approximation for liquids and gases *Int. J. Heat Mass Transfer* **19** 545–51

[10] Martelli D., Venturini A. and Utili M. 2019 Literature review of lead-lithium thermophysical properties *Fusion Eng. Des.* **138** 183–95

[11] Stahl-Eisen-Werkstoffblätter 1992 Physikalische Eigenschaften von Stählen *Stahl-Eisen-Werkstoffblätter des Vereins Deutscher Eisenhüttenleute* (Verlag Stahleisen)

[12] COMSOL COMSOL multiphysics® v. 6.2 (available at: www.comsol.com)

[13] Alberghi C., Candido L., Testoni R., Utili M. and Zucchetti M. 2021 Verification and validation of COMSOL magnetohydrodynamic models for liquid metal breeding blankets technologies *Energies* **14** 5413

[14] Tassone A. 2019 Study on liquid metal magnetohydrodynamic flows and numerical application to a water-cooled blanket for fusion reactors *PhD Thesis* Sapienza University of Rome

[15] ANSYS CFX *Solver Theory Guide* Release 2021R1 (ANSYS Inc.)

[16] Jiang Y., Smolentsev S., Jun J., Pint B. and Kessel C. 2021 Prediction of PbLi fluid flow and temperature field in a thermal convection loop for qualification of fusion materials *Int. J. Heat Mass Transfer* **172** 0017–9310

[17] Suarez D., Khodak A., Mas de Les Valls E. and Batet L. 2022 A formal verification and validation of a low magnetic Reynolds number MHD code for fusion applications *IEEE Trans. Plasma Sci.* **50** 4206–12

[18] Mistrangelo C., Bühler L. and Klüber V. 2023 Towards the simulation of MHD flow in an entire WCLL blanket mock-up *Fusion Eng. Des.* **193** 113752

[19] Zhang X. and Zikanov O. 2014 Mixed convection in a horizontal duct with bottom heating and strong transverse magnetic field *J. Fluid Mech.* **757** 33–56

[20] Oberkampf W. and Trucano T. 2008 Verification and validation benchmarks *Nucl. Eng. Des.* **238** 716–43

[21] Iannone F. *et al* 2019 CRESCO ENEA HPC clusters: a working example of a multifabric GPFS Spectrum Scale layout *Int. Conf. on High Performance Computing & Simulation (HPCS)* (*Dublin, Ireland, 15–19 July 2019*) pp 1051–2 (IEEE)